

Dynamics of stable viscous displacement in porous media

Eyyvind Aker*, Knut Jørgen Måløy

Department of Physics, University of Oslo, N-0316 Oslo, Norway

Alex Hansen

Department of Physics, Norwegian University of Science and Technology, N-7491 Trondheim, Norway

(January 2, 2019)

We investigate the stabilization mechanisms of the invasion front in two-dimensional drainage displacement in porous media by using a network simulator. We focus on the process when the front stabilizes due the viscous forces in the liquids. Especially, we study the variation of the capillary pressure along the front. We find that the capillary pressure difference between two different points along the front vary linearly as function of height separation in the direction of the displacement. Our result is inconsistent with earlier predictions for viscous stabilization when using percolation theory. Instead the behavior of the capillary pressure difference is found to be similar to what is known when gravity stabilizes the front. We also discuss the fluctuations in the capillary pressures between two different points along the front as function of injection rate. Our results are based on a network simulator modeling two phase drainage displacement on a two-dimensional lattice of tubes. We also compare some of our data with experimental work.

47.55.Mh, 07.05.Tp

I. INTRODUCTION

Immiscible displacement of one fluid by another fluid in porous media has important applications in a wide range of different technologies. Most often mentioned is hydrology and oil recovery. From a theoretical point of view, the displacement process is very complex and hard to describe in detail. Especially, much attention has been paid to the rich variety of displacement structures that is observed. The displacement structures are found to depend strongly on the fluid properties like viscosity, interfacial tension, fluid flow rate, and wettability [1,2,3,4].

In drainage displacement the primary process is the displacement of a wetting fluid by a nonwetting fluid in porous media. Consider a two-dimensional horizontal displacement of a less viscous fluid by a more viscous fluid. At high injection rates the front that develops between the invading and defending fluid, is known to stabilize [3]. In contrast, at extremely low injection rate the invading fluid generates a growing cluster similar to the cluster formed by invasion percolation [5,6,7,8]. The displacement is now controlled solely by the capillary pressure P_c , that is the pressure difference between the two fluids across a meniscus.

In this paper we address the question of how the invasion front stabilizes when no gravity forces are present (horizontal displacement). In particular, we will study the temporal evolution of the fluid pressures during the displacement. To do this, we have developed a network model that properly simulates the dynamics of capillary pressure variations along the front as well as the viscous pressure buildup in the fluids. We report that for a wide range of injection rates and different fluid viscosities the capillary pressure P_c along the front, varies linearly in the direction of the displacement. This is a surprisingly sim-

ple result and not expected due to the fractal behavior of the front structure and the non homogeneous viscous force field (see below).

The effect of gravity on the front when the fluids have different densities has been thoroughly discussed [9,10,11,12]. It is found that gravity may stabilize the front in slow drainage. Gravity causes a hydrostatic pressure gradient in the fluids. If a heavy nonwetting fluid is below and displacing vertically upwards a light wetting fluid, this gradient will stabilize the front. The strength of the hydrostatic pressure gradient is often expressed by the bond number, $B_o = \Delta\rho g a^2 / \gamma$, which is the ratio of gravity and capillary forces. Here $\Delta\rho$ denotes the density difference between the fluids, g is the acceleration due to gravity, a is the typical pore size, and γ is the fluid interface tension. The displacement process has been linked to invasion percolation (IP) with a stabilizing gradient [10,11,13]. In IP each site is assigned an invasion probability f . By applying a gradient in the f 's proportional to $-B_o$ the front of the invasion cluster will stabilize. Its saturated front width w_s , has been shown to scale as

$$w_s \propto B_o^{-\nu/(1+\nu)}, \quad (1)$$

where ν is the correlation length exponent from percolation theory ($\nu = 4/3$ in two dimensions).

The understanding of the stabilization process when viscous forces replace the gravity forces is more open. In the literature the mechanisms have been related to IP in a similar manner as the case with gravity [10,14]. However, the scenario is more complicated. Gravity is a uniform force acting on the whole system, while the viscous force is local and fluctuates due to permeability variations and fluid trapping in the porous medium. Percolation concepts have been applied to the displace-

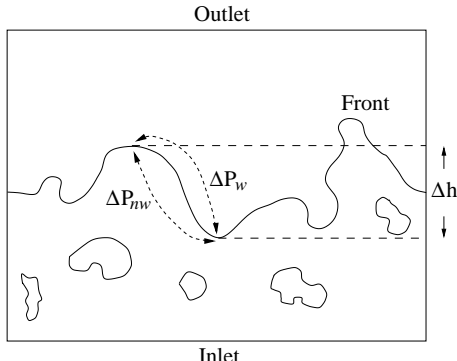


FIG. 1. A schematic picture of the front region that travels across the system from the inlet to the outlet. ΔP_{nw} and ΔP_w denote the pressure drop in the front over the distance Δh in the nonwetting and wetting fluid respectively. The capillary pressure difference between menisci separated a height distance Δh is $\Delta P_{c\parallel} \simeq \Delta P_{nw} - \Delta P_w$. The subscript \parallel , indicates that the capillary pressure difference is calculated in the direction parallel to the displacement.

ment by separating the displacement structure into two parts. One consisting of the frontal region, and the other consisting of the static structure behind. The frontal region of extent w_s , is assumed to behave as the percolating cluster in percolation theory. Consequently, it is assigned the permeability $k \propto w_s^{-t/\nu}$, where t is the conductivity exponent from percolation theory. By applying Darcy's law and assuming that the stabilized front reach a traveling-wave state according to Buckley-Leverett displacement [15], the scaling of the front width is found to behave as [10]

$$w_s \propto C_a^{-\nu/(1+t-\beta+\nu)}. \quad (2)$$

Here β is the order parameter exponent from percolation theory, and C_a denotes the capillary number. In the following $C_a \equiv Q\mu/\Sigma\gamma$, where Q is the injection rate, Σ is the cross section of the inlet, and μ is defined as the maximum viscosity of the two fluids. Physically, C_a is the ratio of viscous to capillary forces.

Wilkinson [10] was the first to propose scaling relation (2) for three dimensional displacement. However, we test it here in two dimensions. In Appendix A we present a simple method to deduce Eq. (2) by applying percolation concepts on the frontal region.

Xu *et al.* [14] went further than Wilkinson and used the percolation approach to deduce a scaling relation for the viscous pressure drop across the front. They proposed that the nonwetting pressure drop ΔP_{nw} across the front should scale as

$$\Delta P_{nw} \propto \Delta h^{t/\nu+d_e-1-\beta/\nu}, \quad (3)$$

over a distance Δh in the direction of the displacement (see Fig. 1). Furthermore, they argued that the corresponding pressure drop in the wetting phase ΔP_w , must

be linearly dependent on Δh since the displaced phase is compact. In Eq. (3) Δh is assumed to be sufficiently large for scaling to be acceptable and less or equal to the front width w_s . Moreover, d_e is the Euclidean dimension of the space embedded by the front. In our case $d_e = 2$.

In this paper we have calculated the capillary pressure variations of the pore menisci along the front in drainage simulations. Especially, we have studied the capillary pressure difference in the direction of the displacement, denoted by $\Delta P_{c\parallel}$. Roughly, $\Delta P_{c\parallel}$ over a height Δh , is given by $\Delta P_{c\parallel} \simeq \Delta P_{nw} - \Delta P_w$ (Fig. 1). Let us assume that the wetting portion to $\Delta P_{c\parallel}$ is small compared to the nonwetting part. This is particularly true at low injection rates and high viscosity contrast between the nonwetting and wetting phase. Then from Eq. (3) we approximate $\Delta P_{nw} \sim \Delta P_{c\parallel} \propto \Delta h^\kappa$ where $\kappa = t/\nu + d - 1 - \beta/\nu$. This is indeed exactly the same result we deduce in Appendix A in two dimensions ($d = 2$). By inserting the value of the exponents in two dimensions, $t = 1.30$, $\beta = 5/36 \simeq 0.14$, and $\nu = 4/3 \simeq 1.33$, we get $\kappa = 1.9$. Our simulation results clearly indicate that $\kappa = 1.0 \pm 0.1$ which is inconstant with the scaling proposed by Xu *et al.* [14].

The paper is organized as follows. In Sec. II we describe the network model used in the simulations. In Sec. III we present and discuss the simulations results and in Sec. IV we compare our results with some experimental data. The conclusions are drawn in Sec. V. At the end we have put Appendix A where we deduce the scaling relation (2).

II. NETWORK MODEL

The network model has been presented elsewhere [16,17] and therefore only its main features will be given here.

In the simulations we have constructed the porous medium in two different ways. In the first way the porous medium is represented by a square lattice of tubes oriented at 45° . The tubes are cylindrical with length d . Each tube is assigned an average radius r which is chosen at random in the interval $[\lambda_1 d, \lambda_2 d]$, where $0 \leq \lambda_1 < \lambda_2 \leq 1$. The randomness of the radii represents the disorder in the system. In the following this system will be referred to as the constant tube length lattice.

In the second way the porous medium is constructed upon a square lattice inclined 45° where the distance between each intersection in the lattice is of unit length. Around each intersection we draw a circle of radius λ . To avoid overlapping circles the given λ must be in the interval $0 \leq \lambda < 1/2$. A node is placed at random inside each of the circles and the nodes inside the nearest neighbor circles are connected by cylindrical tubes. Thus, as for the constant tube length lattice, four tubes meet at each node. We let d_{ij} denote the length of the tube be-

tween the i th and j th node, and the corresponding radius r_{ij} is defined as $r_{ij} = d_{ij}/2\alpha$. Here α is the aspect ratio between the tube length and the radius. In the simulations $\alpha = 1.25$, hence, the tubes are 25% longer than they are wide. In this lattice the position of the nodes represent the disorder in the system, and therefore we will refer to it as the random node lattice.

While every pair of nearest neighbor nodes are separated an equal distance in the constant tube length lattice, the distance between two nearest neighbor nodes vary in the random node lattice. Especially, the shortest length scale, that is the minimum distance between two neighboring nodes, is less in the random node lattice. Consequently, we are able to generate more narrow fronts at higher injection rates at the random node lattice, than what is possible with the constant tube length lattice. Therefore the random node lattice is preferred at high injection rates where a flat front is generated.

In both lattices the tubes represent the volume of both pores and throats. There is no volume assigned to the nodes. The liquids flow from the bottom to the top of the lattice, and we implement periodic boundary conditions in the horizontal direction. The pressure difference between the bottom row and the top row defines the pressure across the lattice. Initially, the system is filled with a wetting fluid with viscosity μ_w . The injected fluid is nonwetting and has viscosity $\mu_{nw} \geq \mu_w$. The viscosity ratio M , is defined as $M \equiv \mu_{nw}/\mu_w$.

The capillary pressure p_c between the nonwetting and wetting fluid in a tube is given by Young-Laplace law

$$p_c = \gamma \left(\frac{1}{R_1} + \frac{1}{R_2} \right), \quad (4)$$

where R_1 and R_2 are the principal radii of curvature of the interface (a meniscus) and γ is the interfacial tension. In a cylindrical tube of radius r where $R_1 = R_2$, Eq. (4) reduces to $p_c = (2\gamma/r) \cos \theta$. Here θ denotes the wetting angle between the nonwetting and wetting phases, and in drainage θ is in the interval $(0, \pi/2)$.

In the network model we treat the tubes as if they were hourglass shaped with effective radii following a smooth function. Hence, we let the capillary pressure become a function of the meniscus position in the tube and assume the Young-Laplace law (4) takes the form

$$p_c = \frac{2\gamma}{r} [1 - \cos(2\pi \frac{x}{d})]. \quad (5)$$

Here $0 \leq x \leq d$ is the position of the meniscus in the tube where d is the tube length. We assume perfect wetting, i.e. $\theta = 0$.

By letting p_c vary according to (5), we include the effect of burst dynamics into the model [16]. This is particularly seen at low injection rates where the invasion of nonwetting fluid takes place in bursts accompanied by sudden negative jumps in the pressure (Haines jumps) [18,19]. The detailed modelling of the capillary

pressure costs computation time. However, it seems necessary in order to properly simulate the pressure behavior along the front.

The volume flux q_{ij} through a tube from the i th to the j th node is found from the Washburn equation for capillary flow [20]

$$q_{ij} = -\frac{\sigma_{ij} k_{ij}}{\mu_{ij}} \frac{1}{d} (\Delta p_{ij} - p_c). \quad (6)$$

Here k_{ij} is the permeability of the tube ($r_{ij}^2/8$) and σ_{ij} is the cross section (πr_{ij}^2) of the tube. μ_{ij} is the effective viscosity given by the sum of the volume fractions of each fluid inside the tube multiplied by their respective viscosities. The pressure drop across the tube is $\Delta p_{ij} = p_j - p_i$, where p_i and p_j is the nodal pressures at node i and j respectively. The capillary pressure p_c is the sum of the capillary pressures of the menisci (given by Eq. (5)) inside the tube. A tube partially filled with both liquids, is allowed to contain either one or two menisci. For a tube without menisci $p_c = 0$, and Eq. (6) reduces to that describing Hagen-Poiseuille flow with $\mu_{ij} = \mu_1$ or μ_2 .

No volume assigned to the nodes, giving conservation of volume flux at each node

$$\sum_j q_{ij} = 0. \quad (7)$$

The summation on j runs over the nearest neighbor nodes to the i th node while i runs over all nodes that do not belong to the top or bottom rows, that is, the internal nodes.

Eqs. (6) and (7) constitute a set of linear equations which are to be solved for the nodal pressures p_j , with the constraint that the pressures at the nodes belonging to the upper and lower rows are kept fixed. The set of equations is solved by using the Conjugate Gradient method [21].

We want to solve the p_j 's for an applied constant injection rate Q giving a time dependent pressure ΔP across the lattice. To do this, we use a relation between the nodal pressures p_j and ΔP which goes as $\Delta p_{ij} = \Gamma_{ij} \Delta P + \Pi_{ij}$ [16,17]. Here Γ_{ij} is a dimensionless quantity depending on the mobilities (k_{ij}/μ_{ij}) of the tubes and Π_{ij} is a function of the capillary pressures of the menisci inside the tubes. If no menisci in the network are present Π_{ij} is zero. ΔP is calculated by inserting the desired flux into the functional relation $\Delta P = \mathcal{A}Q + \mathcal{B}$ [16,17]. Here \mathcal{A} and \mathcal{B} is found by inserting the calculated fluxes Q' and Q'' corresponding to the solution of Eq. (7) for two different pressures $\Delta P'$ and $\Delta P''$ applied across the lattice. According to [17] \mathcal{A} should be read as the total resistance of the system and \mathcal{B} is the pressure drop due to the capillary pressure of the menisci.

Summarized, the procedure for each time step Δt is:

(1) Solving Eqs. (6) and (7) twice for two different pressures $\Delta P'$ and $\Delta P''$, applied across the lattice. This gives us two sets of the nodal pressures p_{ij} .

(2) Calculate the corresponding fluxes Q' and Q'' , from the solutions in step (1) and find \mathcal{A} and \mathcal{B} .

(3) Use $\Delta P = \mathcal{A}Q + \mathcal{B}$ to find the pressure ΔP across the lattice by inserting the given injection rate Q .

(4) Calculate the nodal pressures p_{ij} due to this ΔP by using $\Delta p_{ij} = \Gamma_{ij}\Delta P + \Pi_{ij}$. Note that Γ_{ij} and Π_{ij} is already known from the two solutions from step (1).

(5) The local flow rate q_{ij} in each tube is computed by using Eq. (6) and the nodal pressures p_{ij} from step (4).

(6) Calculate a time step Δt , such every meniscus is allowed to travel at most a maximum step length Δx_{\max} , during every time step.

(7) The menisci are updated according to the found q_{ij} and Δt . The total time lapse is recorded before the whole procedure is repeated for the new fluid configuration.

Numerical simulations show that Δx_{\max} must be of order 0.1 to calculate the variation in the capillary pressure when a meniscus travel through a tube. In all simulations presented here $\Delta x_{\max} = 0.1$, resulting in at least ten time steps to invade one tube with nonwetting fluid. This causes the computation time to increase dramatically.

Menisci that are moved out of a tube during a time step are spread into neighbor tubes. For details about how the menisci is moved into neighbor tubes see Refs. [16] and [17].

III. SIMULATIONS

We have run drainage displacement simulations at different injection rates to study the dependency of the front structure on the capillary pressure variations along the front. Due to the huge computational effort, the simulations have been limited to lattices of size 25×35 and 40×60 nodes. We have also run displacement simulations that were initiated on clusters which were generated by an invasion percolation algorithm. In this way, we were able to study the capillary pressure variations along the invasion front on lattices of size 200×300 nodes.

In each simulation the front between the nonwetting invading fluid and the defending wetting fluid was detected by running a Hoshen-Kopelman algorithm [22] on the lattice. The typical displacement structures obtained at different capillary numbers on the lattices of 40×60 nodes, is shown in Fig. 2. The front is defined as the set of tubes that contain a front meniscus between the nonwetting and wetting phase. At low C_a we approach the limit of capillary fingering where the invading fluid creates a rough front with trapped cluster on all sizes between the maximum front width and the tube length. At high C_a the front stabilize and a typical compact pattern with a flat front generates.

The variation of the capillary pressure ΔP_c , between pairs of menisci along the front was calculated. ΔP_c was found both in the direction of the displacement denoted by $\Delta P_{c\parallel}$, and in the orthogonal direction given as

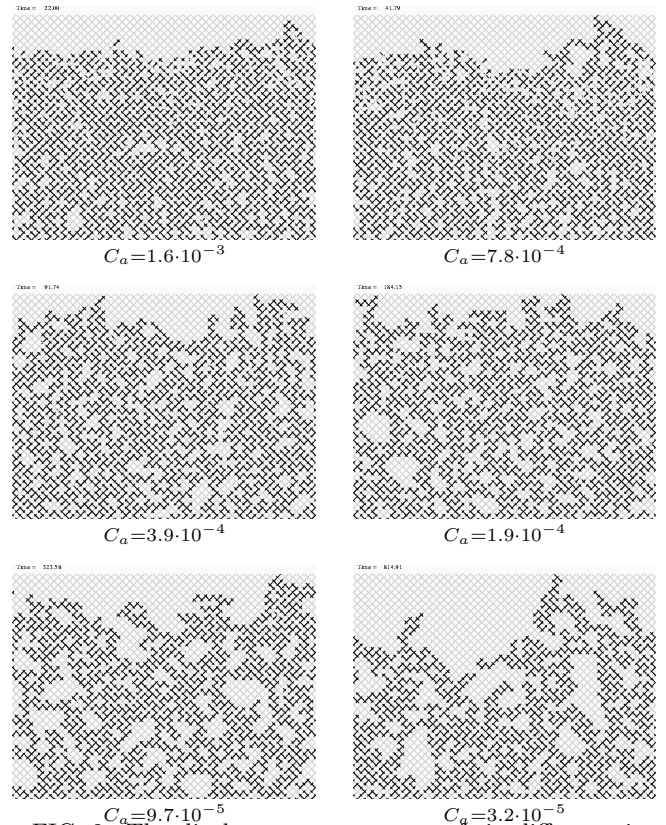


FIG. 2. The displacement structures of six different simulations at breakthrough. The simulations were done on the lattice of 40×60 nodes and $M = 1$. The structure of the simulation at $C_a = 3.2 \times 10^{-5}$ shows a wide front with trapped clusters on many length scales. The simulations at $C_a = 1.6 \times 10^{-3}$ shows a compact pattern with a narrow front and corresponding small trapped clusters. The black nonwetting fluid displaces the gray wetting fluid from below.

$\Delta P_{c\perp}$. In Fig. 1 we have given an approximate definition of $\Delta P_{c\parallel}$. Below, we describe the exact definitions of $\Delta P_{c\parallel}$ and $\Delta P_{c\perp}$, used in the simulations. Consider two front menisci denoted by m and n with height h_m and h_n above the inlet (bottom row) at a distance l_m and l_n from the left boundary of the lattice. Assume that $h_m > h_n$, then we define the difference $\Delta P_c^{mn}(\Delta h, \Delta l) = p_c^n - p_c^m$ where $\Delta h = |h_m - h_n|$ and $\Delta l = |l_m - l_n|$. If instead $h_n > h_m$, we compute $\Delta P_c^{nm}(\Delta h, \Delta l) = p_c^m - p_c^n$. We only consider the front tubes that contain one meniscus and where the nonwetting fluid invades the tube from below. The capillary pressure difference in the direction of the displacement $\Delta P_{c\parallel}$, as function of Δh , is defined as the average of ΔP_c^{mn} over all pairs mn separated a distance Δh but different Δl , i.e. $\Delta P_{c\parallel} = \langle \Delta P_c^{mn}(\Delta h = \text{const.}, \Delta l) \rangle$.

The capillary pressure difference in the orthogonal direction, $\Delta P_{c\perp}$, (parallel to the inlet) as function of Δl is defined as the average of $|\Delta P_c^{mn}|$ over all pairs mn with equal height ($\Delta h = 0$) above the inlet when Δl is held constant. Thus, in the above notation $\Delta P_{c\perp} = \langle |\Delta P_c^{mn}(0, \Delta l = \text{const.})| \rangle$.

For each simulation we also recorded the front width w . The front width was defined as the standard deviation of the distances between all the front tubes and the average position of the front.

The simulations were performed with parameters as close as possible to experiments performed in [23]. In the lattice of constant tube lengths we assigned the length d , of all tubes equal to 1 mm and the radii r of the tubes were randomly chosen in the interval $0.05d \leq r \leq d$. In the lattices with random nodes we chose the positions of the nodes such that the length of the tubes were inside the interval $0.2 \leq d \leq 1.8$ mm. This gave us the radii of the tubes, defined by $r = d/2\alpha$, where $\alpha = 1.25$. For both types of lattices the interfacial tension was set to $\gamma = 30$ dyn/cm, and the fluid viscosities were 0.010 P, 0.50 P or 10 P.

A. Viscosity ratio, $M = 100$

We have performed two series of simulations with viscosity ratio $M = 100$, going from low to high injection rate. In the first series we used the constant tube length lattice, and in the second series the simulations were done on the random node lattice. In both series the lattice size was 25×35 nodes. In Tables I and II we have listed the injection rates and capillary numbers used in the simulations done on the constant tube length lattice (Table I) and the random node lattice (Table II). Also shown are the recorded saturated front width and the number of different runs we did at each injection rate.

The capillary pressure difference in the direction of the displacement, $\Delta P_{c\parallel}$, and in the orthogonal direction, $\Delta P_{c\perp}$, was recorded for all simulations. The result for $\Delta P_{c\parallel}$ of the series performed on the constant tube length lattice, is shown in Figs. 3 and 4.

TABLE I. Simulations performed on the constant tube length lattice of size 25×35 nodes and $M = 100$. The table contains the number of runs at each injection rate Q , the corresponding capillary number C_a , and the saturated front width w_s .

Runs	Q (cm ³ /min)	C_a	w_s
30	0.050	3.7×10^{-4}	5.5 ± 0.5
30	0.10	7.3×10^{-4}	4.3 ± 0.4
30	0.20	1.5×10^{-3}	3.7 ± 0.4
30	0.50	3.7×10^{-3}	3.0 ± 0.3
30	0.80	5.8×10^{-3}	2.5 ± 0.3
30	1.5	1.1×10^{-2}	2.4 ± 0.2

TABLE II. Simulations performed on the random node lattice of size 25×35 nodes and $M = 100$. The table contains the number of runs at each injection rate Q , the corresponding capillary number C_a , and the saturated front width w_s .

Runs	Q (cm ³ /min)	C_a	w_s
10	0.010	1.0×10^{-4}	4.3 ± 0.6
20	0.030	3.1×10^{-4}	2.9 ± 0.3
20	0.050	5.2×10^{-4}	2.5 ± 0.2
20	0.10	1.0×10^{-3}	2.1 ± 0.2
20	0.30	3.1×10^{-3}	1.4 ± 0.1
15	0.50	5.2×10^{-3}	1.2 ± 0.1
15	1.0	1.0×10^{-2}	0.9 ± 0.1
10	2.0	2.1×10^{-2}	0.8 ± 0.1
10	4.0	4.2×10^{-2}	0.8 ± 0.1

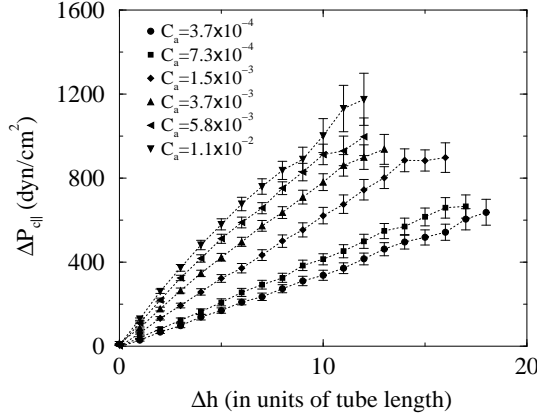


FIG. 3. $\Delta P_{c\parallel}$ as function of Δh in the direction of displacement for various C_a and $M = 100$. At each C_a , $\Delta P_{c\parallel}$ is the average of 30 different runs and the error bars denote the standard error of the mean.

In the logarithmic plot in Fig. 4 we have fitted the results to a straight line for $C_a = 3.7 \times 10^{-4}$ and $C_a = 1.1 \times 10^{-2}$. Assuming a power law behavior, we find that at $C_a = 3.7 \times 10^{-4}$, $\Delta P_{c\parallel} \propto \Delta h^\kappa$ where $\kappa = 1.0$. The exponent κ seems to decrease systematically with increasing injection rate, and at $C_a = 1.1 \times 10^{-2}$ our best estimate is $\kappa = 0.8$. Similar results were found from the simulations performed on the random node lattice. The data points corresponding to $\Delta h \leq 1$ tube length is omitted in the calculations of the exponent in Fig. 4. At short distances we expect uncertainties in the result because of the finite length of the tubes in the lattice.

In Fig. 3 we observe that $\Delta P_{c\parallel}$ increases more rapidly as function of Δh at high injection rates compared to the results at low injection rates. At extremely low injection rate we expect $\Delta P_{c\parallel}$ in Fig. 3 to approach zero and become independent of Δh . In this limit the capillary pressure of the menisci along the front are equal (capillary equilibrium). As seen from Fig. 3, we have not performed simulations with that low injection rate. Instead the lowest capillary number in Fig. 3 corresponds to the injection rate where no clear stabilization of the front was found due to the finite size of the system.

At higher injection rates the viscous gradient stabilizes the front. The gradient results the capillary pressure of the menisci closest to the inlet to exceed the capillary pressure of the menisci lying in the uppermost part. Thus, the menisci closest to the inlet will easier penetrate a narrow tube compared to menisci further down the stream. This will eventually stabilize the front. The viscous pressure gradient will increase with increasing injection rate, resulting in a more narrow front width. This is seen in Tables I and II where w_s was found to decrease with increasing C_a .

In Fig. 5 we have plotted the average position $\langle x \rangle$, of the front menisci inside the tubes as function of

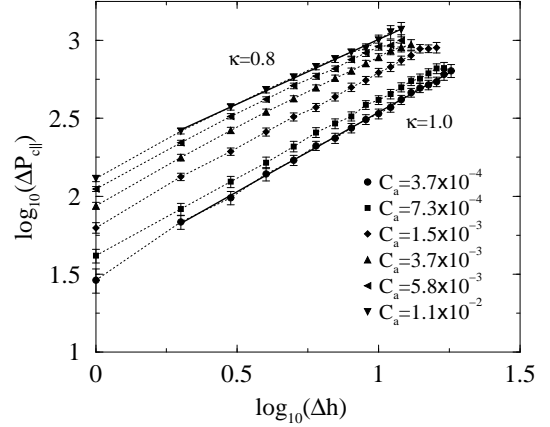


FIG. 4. $\log_{10}(\Delta P_{c\parallel})$ as function of $\log_{10}(\Delta h)$ in the direction of displacement for various C_a and $M = 100$. At each C_a , $\Delta P_{c\parallel}$ is the average of 30 different runs and the error bars denote the standard error of the mean. The solid lines were fitted to the result at $C_a = 1.1 \times 10^{-2}$ and 3.7×10^{-4} . The slope of the lines are given by κ in the figure.

their vertical height h , relative to the bottom height of the front, h_{\min} . From Fig. 5 we observe that at high $C_a = 1.0 \times 10^{-2}$ where the viscous pressure gradient is strong, the menisci behind in the front is placed closer to the middle of the tube compared to the menisci ahead. Consequently, the capillary pressure of the menisci behind is larger than the capillary pressure of the menisci ahead and therefore tubes behind will more easily be invaded. Remember that the tubes are hourglass shaped and that the most narrow part of the tube is at $x = 0.5$ (see Eq. (5)). At low injection rate ($C_a = 1.0 \times 10^{-4}$) we approach the regime of capillary equilibrium giving almost no difference in $\langle x \rangle$ as function of $h - h_{\min}$.

In Fig. 3 the value of $\Delta P_{c\parallel}$ at $\Delta h = w_s$, denoted as $\Delta P_{c\parallel}(w_s)$, tend to increase with increasing C_a . In gravitational stabilization $\Delta P_{c\parallel}(w_s) \propto w_s B_o \sim B_o^{1/(1+\nu)}$ [11]. Note that $w_s \propto \xi$ is the correlation length in percolation theory. According to Wilkinson [10] the viscous analog should read $\Delta P_{c\parallel}(w_s) \propto C_a^{1/(1+t-\beta+\nu)}$. By inserting the values of the exponents in two dimensions, we get $\Delta P_{c\parallel}(w_s) \propto C_a^{0.29}$. Fig. 6 shows a log-log plot of $\Delta P_{c\parallel}(w_s)$ as function of C_a for the simulations done on the random node lattice. From the plot it is difficult to estimate the exponent, but if we assume a power law behavior our best result is 0.15 ± 0.05 . We find similar result for the simulations performed on the constant tube length lattice.

From Fig. 6 there seems to be an upper cut off at $C_a \gtrsim 1.0 \times 10^{-2}$ where $\Delta P_{c\parallel}(w_s)$ stops growing. At $C_a \gtrsim 1.0 \times 10^{-2}$ the front is typically flat and we approach the minimum width due to the finite length of the tubes (see Table II). In this limit we expect a cross over to another type of scaling behavior.

In gravitational stabilization the injection rate is kept

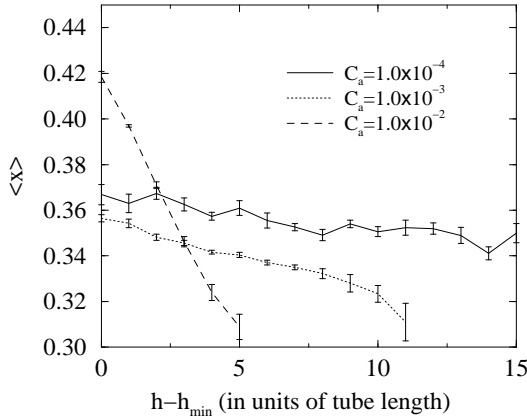


FIG. 5. The average position $\langle x \rangle$, of the front menisci inside the tubes as function of the menisci's height h relative to the of bottom of the front h_{\min} . The lattice used was the random node lattice of size 25×35 nodes with $M = 100$.

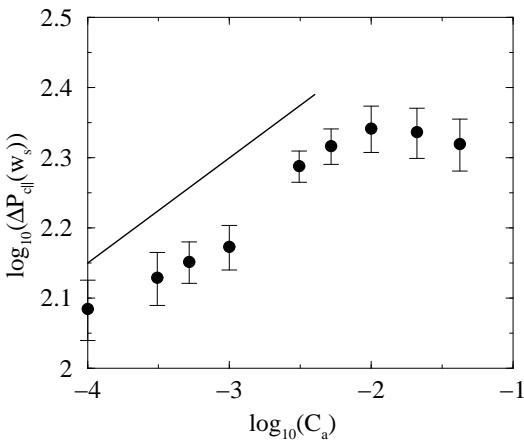


FIG. 6. $\log_{10}(\Delta P_{c\parallel}(w_s))$ as function of $\log_{10}(C_a)$ for the simulations done at the random node lattice. The lattice size was 25×35 and $M = 100$. The slope of the solid line is 0.15. The error bars denote the standard error in the mean.

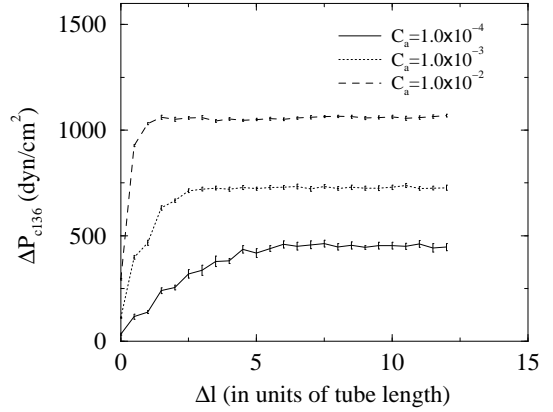


FIG. 7. The absolute capillary pressure difference in the orthogonal direction $\Delta P_{c\perp}$, as function of the horizontal distance Δl for three different capillary numbers. The simulations were run on the random node lattice with $M = 100$. The lattice size was 25×35 , giving a maximum horizontal distance $\Delta l = 12.5$ due to the periodic boundary conditions. The error bars denote the standard error in the mean.

low to eliminate the viscous forces. Thus, the system exhibits capillary equilibrium along the front and the invasion of nonwetting fluid occurs in a series of bursts [24]. The time step of a burst is very short compared to the slow injection rate. Therefore, the volume of wetting fluid that is displaced when nonwetting fluid enters a new pore in a burst, must be compensated by a retraction of the front in neighboring tubes. The front menisci will quickly readjust back to larger radii and the capillary pressure will decrease in a jump (Haines jumps) [18].

In viscous stabilization at high injection rate, the system will not be in capillary equilibrium at all. Eventually, the injection rate will be high enough to prevent the menisci to readjust in the close vicinity of a burst. Consequently, new pores will be invaded simultaneously everywhere along the front.

This is demonstrated in Fig. 7, where we have plotted the capillary pressure difference in the orthogonal direction, $\Delta P_{c\perp}$, for the simulations performed on the random node lattice. $\Delta P_{c\perp}$ is the absolute capillary pressure difference between menisci at same height above the inlet but separated a horizontal distance Δl . We interpret it as the horizontal correlations in the capillary pressure between menisci at same height. Recall that $\Delta P_{c\perp}$ contains terms like $|p_c^m - p_c^n| = \sqrt{(p_c^m - p_c^n)^2}$ where p_c^m and p_c^n denote the capillary pressure of two front menisci m and n (see beginning of Sec. III). From Fig. 7 we see that at low C_a the capillary pressure of two menisci at same height and a distance $\Delta l \lesssim 7$ apart, are correlated to each other because $\Delta P_{c\perp}$ depends on Δl . Above $\Delta l = 7$, $\Delta P_{c\perp}$ approaches a constant, meaning that the capillary pressures of the menisci do no longer interfere. At high $C_a = 1.0 \times 10^{-2}$, we observe that the correlations are very short. Already for $\Delta l > 1$, $\Delta P_{c\perp}$ becomes a constant and

TABLE III. Simulations performed on the random node lattice of size 40×60 nodes and $M = 1$. The table contains the number of runs at each injection rate Q , the corresponding capillary number C_a and the saturated front width w_s .

Runs	Q (cm^3/min)	C_a	w_s
10	0.050	1.6×10^{-5}	7.5 ± 1.5
10	0.10	3.2×10^{-5}	6.9 ± 1.2
15	0.30	9.7×10^{-5}	5.2 ± 0.5
15	0.60	1.9×10^{-4}	4.4 ± 0.5
20	1.2	3.9×10^{-4}	3.8 ± 0.5
20	2.4	7.8×10^{-4}	3.0 ± 0.2
20	4.8	1.6×10^{-3}	2.4 ± 0.2

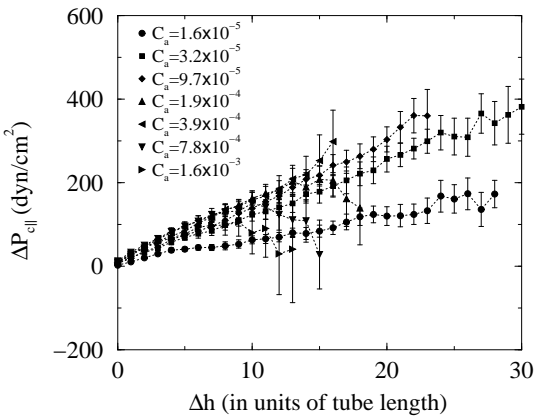


FIG. 8. $\Delta P_{c\parallel}$ as function of Δh in the direction of displacement for the different C_a on the lattice of 40×60 nodes. The fluid had equal viscosities ($M = 1$). $\Delta P_{c\parallel}$ is the average of the different runs at each C_a and the error bars denote the standard error of the mean.

the capillary pressures of the menisci are uncorrelated. Thus, if we consider a narrow and a wide tube at same height, the viscous forces are strong enough to push the nonwetting fluid through both the narrow and the wide tube simultaneously. As a result nonwetting fluid will invade everywhere along the front. We will later refer to this as dispersive growth of the front. In Fig. 7 only the results of the simulations performed on the random node lattice is shown. However, similar behavior was observed when the constant tube length lattice was applied.

B. Viscosity ratio, $M = 1$

We have run a series of simulations with equal viscosities, $M = 1$, on the random node lattice of size 40×60 nodes. The different injection rates, capillary numbers, the measured saturated front width and the number of runs at each injection rate, are listed in table Table III.

Fig. 8 shows the calculated $\Delta P_{c\parallel}$ as function of Δh in the direction of the displacements. As for the case with

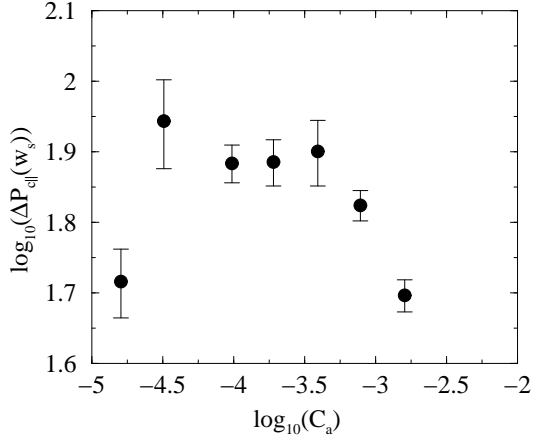


FIG. 9. $\log_{10}(\Delta P_{c\parallel}(w_s))$ as function of $\log_{10}(C_a)$ for the simulations done at the random node lattice. The lattice size was 40×60 nodes and $M = 1$. The error bars denote the standard error of the mean.

$M = 100$, $\Delta P_{c\parallel}$ is expected to approach a constant when C_a goes to zero. In Fig. 9 we have plotted the logarithm of $\Delta P_{c\parallel}(w_s)$ versus the logarithm of C_a . From Figs. 8 and 9 we note that already for $C_a \gtrsim 1 \times 10^{-4}$, $\Delta P_{c\parallel}(w_s)$ reaches a plateau or even decreases and we can not see any power law behavior. This is quite different from what we observed in Fig. 6 for $M = 100$.

To explain the different behavior of $\Delta P_{c\parallel}(w_s)$ when $M = 100$ and $M = 1$, we first look at the capillary pressure gradient across the front and second we compare that to $\Delta P_{c\perp}$.

In Fig. 10 we have plotted the average capillary pressure $\langle P_c \rangle$, in the frontal region as function of the height h relative to the bottom height of the front, h_{\min} . $\langle P_c \rangle$ was calculated by taking the average of the capillary pressures of the front menisci at same height above the inlet. In Fig. 10 the result of two different simulations at almost same C_a , are shown. One corresponding to the random node lattice of 25×35 nodes with $M = 100$ and $C_a = 1.0 \times 10^{-3}$, and the other given by the random node lattice of 40×60 nodes with $M = 1$ and $C_a = 1.6 \times 10^{-3}$. If we consider the middle part of the front between the two vertical dashed lines in Fig. 10, we observe that the capillary pressure drop across the front, $-w_s d\langle P_c \rangle / dh$, is higher for $M = 100$ than for $M = 1$, even though the capillary numbers are almost equal. In both simulations in Fig. 10, a typical narrow front with a compact displacement structure developed. Thus, when the nonwetting and wetting fluid have equal viscosities ($M = 1$) the pressure drop in the compact structure becomes almost equal to the pressure drop in the wetting phase. When $M = 100$ however, the pressure drop in the compact structure is much larger than in the wetting phase, due to the higher viscosity of the nonwetting fluid. The capillary pressure drop across the front is given by the difference in pressure drops between the nonwetting and

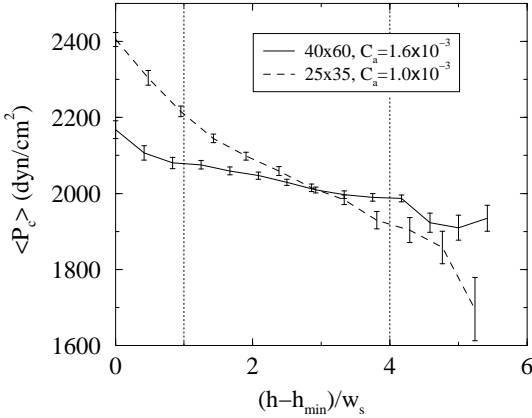


FIG. 10. $\langle P_c \rangle$ in the frontal region as function of the height distance relative to the bottom height of the front h_{\min} . The height distance is normalized by dividing with the saturated front width w_s . The vertical dashed lines indicate the region where $\langle P_c \rangle$ is approximately linear. The error bars denote the standard error of the mean.

wetting phase (see for instance Fig. 1). Consequently, $-w_s d\langle P_c \rangle / dh$ for a given C_a must be lower when $M = 1$ than when $M = 100$, as the results in Fig. 10 shows.

Let us now study the behavior of $\Delta P_{c\perp}$ when $M = 1$. Physically, $\Delta P_{c\perp}$ is the amplitude of the capillary pressure fluctuations due to the different positions of the menisci in the tubes at the same vertical height above the inlet. Simulations show, that for the same C_a we obtain almost identical results for $\Delta P_{c\perp}$ when $M = 100$ and $M = 1$. Especially, the plateau where the capillary pressures are uncorrelated has the same value. To illustrate this we have plotted the plateau of $\Delta P_{c\perp}$ versus C_a in a logarithmic plot in Fig. 11. The data corresponds to the simulations performed on the random node lattices of 25×35 nodes and $M = 100$ (Table II), and the random node lattice of 40×60 nodes with $M = 1$ (Table III). As a guidance to the eye we have drawn a straight line in Fig. 11, to indicate that there might be a power law behavior between the plateau of $\Delta P_{c\perp}$ and C_a . The slope of the line is 0.2.

From the above discussion we draw the following conclusion. Consider two rows of front tubes, separated a vertical distance equal to the front width w_s . When $M = 1$ the capillary pressure drop between the rows is small due to the equal fluid viscosities (Fig. 10). However, the amplitudes of the capillary fluctuations, $\Delta P_{c\perp}$, are the same as when $M = 100$ (Fig. 11). Thus, when $M = 1$ the relative small capillary pressure drop between the rows is annihilated by the capillary pressure fluctuations. This destroys the power law behavior of $\Delta P_{c\parallel}(w_s)$ in Fig. 9. When $M = 100$, the capillary fluctuations are too small to annihilate the larger capillary pressure drop there, giving the increasing function $\Delta P_{c\parallel}(w_s)$ in Fig. 6. If we divide the capillary pressure drop, calculated in Fig. 10, with the plateau of $\Delta P_{c\perp}$, we find that the ratio

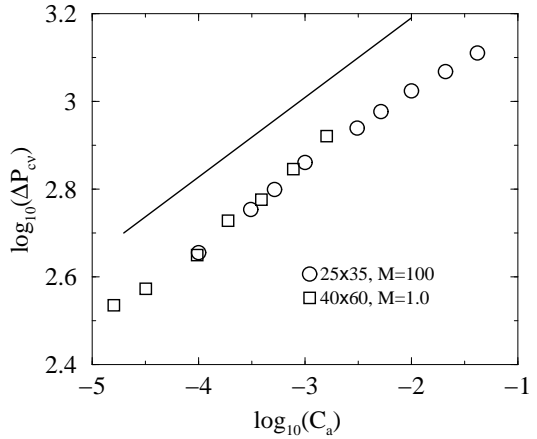


FIG. 11. The logarithm of the plateau of $\Delta P_{c\perp}$ versus the logarithm of C_a . The result of the random node lattice of 25×35 nodes and $M = 100$ is plotted as circles while the result of the random node lattice of 40×60 nodes with $M = 1$ is plotted as boxes. The slope of the solid line is 0.2.

is a factor three lower for $M = 1$ than for $M = 100$ at $C_a \simeq 1.0 \times 10^{-3}$.

In Fig. 12 we have plotted the logarithm of $\Delta P_{c\parallel}$ versus the logarithm of Δh at $C_a = 3.2 \times 10^{-5}$ and 7.8×10^{-4} . For large front widths at $C_a = 3.2 \times 10^{-5}$, we estimate $\kappa = 1.0 \pm 0.1$ if we assume a scaling behavior like $\Delta P_{c\parallel} \propto \Delta h^\kappa$. At smaller distances we observe a cross over to a slightly lower exponent, $\kappa = 0.8 \pm 0.1$. For $C_a = 7.8 \times 10^{-4}$ our best estimate is $\kappa = 0.7 \pm 0.1$. In this simulation the front width is too narrow to reach the scaling regime where $\kappa = 1.0$. Due to the finite length of the tubes we expect the scaling relation to change when Δh approaches the length of the tubes. This might also explain the systematic change in the exponent that we found in Fig. 3. From Figs. 3 and 8 we conclude that for sufficient wide fronts, $\Delta P_{c\parallel} \propto \Delta h^{1.0 \pm 0.1}$.

C. Invasion percolation cluster

In order to increase the size of the lattices we generated invasion percolation (IP) clusters with a stabilizing gradient. The IP clusters were then loaded into our network model, and the displacement process was initiated on this structure. Using this method, we were able to perform displacements in a short period of time on IP clusters generated on lattices of size 200×300 . The result of these simulations are based on the assumption that the generated IP structures are statistically equal to the structures that would have been obtained in a corresponding complete displacement process.

The IP algorithm was performed on the bonds in a square lattice with the bonds oriented at 45° . Hence, the bonds correspond to the tubes in our original network model. Each bond were assigned a random number f_{ij} in

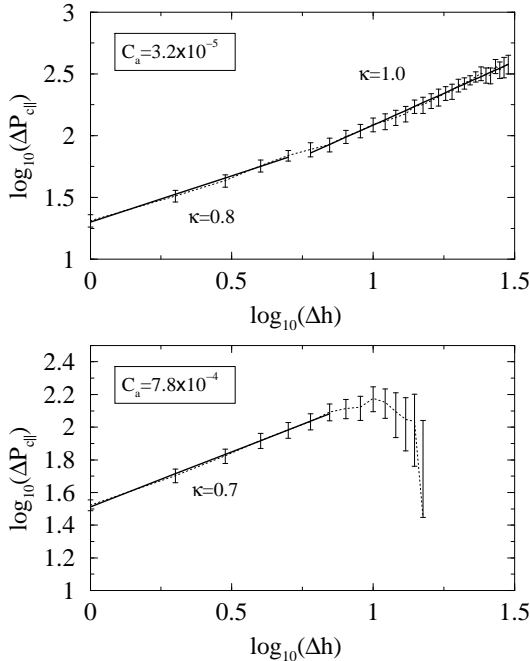


FIG. 12. $\log_{10}(\Delta P_{c\parallel})$ as function of $\log_{10}(\Delta h)$ averaged over the different simulations at $C_a = 3.2 \times 10^{-5}$ (above) and $C_a = 7.8 \times 10^{-4}$ (below). The error bars denote the standard error of the mean. The lattice size was 40×60 nodes and $M = 1$. The solid lines were fitted to the data and their slope is given by κ .

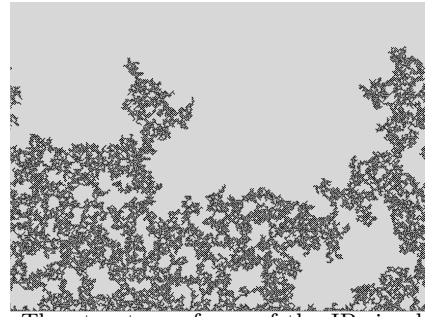


FIG. 13. The structure of one of the IP simulations with the gradient $G = 0.05$. The structure was loaded into our network model and the lattice size was 200×300 .

the interval $[0, 1]$ where ij denote the bond between the i th and the j th node in the lattice. A stabilizing gradient G , was applied on the lattice giving an occupation threshold t_{ij} of every bond, $t_{ij} = f_{ij} + Gh_{ij}$ [10,11]. Here h_{ij} denotes the height of bond ij above the bottom row. The occupation of bonds started at the bottom row, and new bonds were occupied until the invasion cluster reached the top row. There was periodic boundary conditions in the horizontal direction. The next bond to be occupied was defined as the bond with the lowest threshold value t , from the set of empty bonds along the invasion front. The invasion front was found by running a Hoshen-Kopelman algorithm on the lattice.

We ran four IP simulations with $G = 0.05$ and different sets of random numbers f . When the invasion front became well developed with cluster of all sizes between the size of the bonds and the front width, the structures were loaded into our network model. Fig. 13 shows one of the IP structures that was generated.

When the IP structures were loaded into our network model, the radii r_{ij} of the tubes in the lattice were mapped to the random numbers f_{ij} of the bonds like $r_{ij} = [\lambda_1 + (\lambda_2 - \lambda_1)(1 - f_{ij})]d$. Thus, $r_{ij} \in [\lambda_1 d, \lambda_2 d]$ where as earlier, the tube length $d = 1$ mm, $\lambda_1 = 0.05$ and $\lambda_2 = 1.0$. Note that the radii of the tubes are mapped to $1 - f_{ij}$ because in the IP algorithm the next bond to be invaded is the one with the lowest threshold value, opposite to the network model, where the widest tubes will be invaded first.

In the network model the invasion of nonwetting fluid is controlled by the threshold capillary pressures p_t of the tubes. According to Eq. (5) $p_t = 4\gamma/r$ in the middle of the tubes where $x = d/2$. In the IP model the distribution of the random numbers f , is flat. Thus, when the radii r of the tubes in the network model are mapped to the f 's we obtain a $1/p_t^2$ distribution of capillary pressure thresholds. However, since there is a one to one correspondence in the mapping from the set of f 's to the set of p_t 's, we can assume that the IP structures are statistically equal to similar structures that would have been generated in a full displacement simulation. The as-

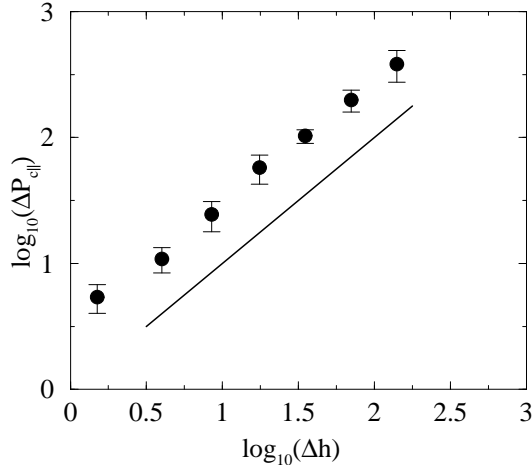


FIG. 14. $\log_{10}(\Delta P_{c\parallel})$ as function of $\log_{10}(\Delta h)$ for simulations initiated on IP structures. The result is averaged over four different IP structures and the error bars denote the standard error in the mean. The lattice size was 200×300 and the viscosity ratio $M = 100$. The slope of the straight solid line is 1.0.

sumption provides that the displacement simulations is performed with an appropriate injection rate Q , according to G that was used to generate the IP structures.

After the network model was initiated by the IP structures, we ran displacement simulations on the structures a limited number of time steps and recorded $\Delta P_{c\parallel}$. The number of time steps were chosen such that the front menisci got sufficient time to adjust according to the viscous pressure set up by the injection rate. For all four structures we chose $M = 100$ and $Q = 0.2 \text{ ml/min}$ giving $C_a = 1.8 \times 10^{-4}$. This capillary number might be too high compared to the front widths and capillary numbers listed in Tables I and II. The reason why we choose a high C_a is to minimize computation time. Simulations show that fewer time steps and hence less CPU time are needed to adjust the front menisci when a higher injection rate is applied instead of a low one. Moreover, the simulations also show that as long as the number of time steps are chosen sufficiently large to allow the front menisci to adjust, the exponent κ in $\Delta P_{c\parallel} \propto \Delta h^\kappa$, is not sensitive on the injection rate. In the present simulations the number of time steps was 400.

The result of the simulations performed on the IP structures is shown in Fig. 14 where we have plotted $\log_{10}(\Delta P_{c\parallel})$ versus $\log_{10}(\Delta h)$. As for the previous results we find $\kappa = 1.0 \pm 0.1$. The slope of the straight line in Fig. 14 is 1.0. We have also done displacement simulations on IP structures with $M = 1$. The result of these simulations are similar to those we observe in Fig. 14.

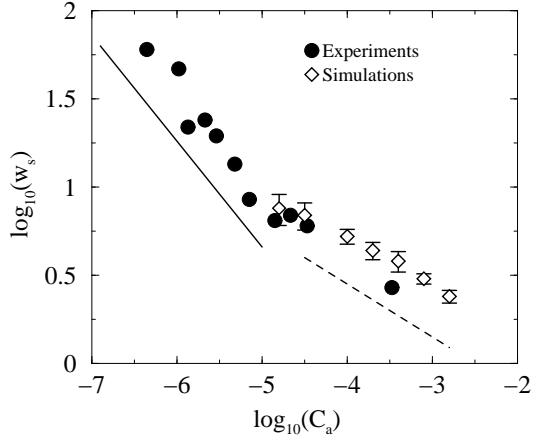


FIG. 15. $\log_{10}(w_s)$ as function of $\log_{10}(C_a)$ for experiments from [23] and simulations on the lattice of 40×60 nodes. For both experiments and simulations $M = 1$. The slope of the solid and dashed line is -0.6 and -0.3 respectively. For the simulations, the width w_s and the standard error of w_s are listed in Table III.

IV. COMPARISON WITH EXPERIMENTS

Frette *et al.* [23] performed two phase drainage displacement experiments in a two-dimensional porous medium with viscosity matched fluids. They reported on the stabilization of the front and measured the saturated front width w_s as function of capillary number. In all our simulations except those performed on the IP cluster, we calculated w_s (see Tables I, II and III) According to [10,14] w_s should scale with C_a as in Eq. (2).

In Fig. 15 we have plotted w_s versus C_a in a logarithmic plot. The plot shows the experimental data of Frette *et al.* and the results of our simulations on the lattice of 40×60 nodes. Both in the experiments and in the simulations viscosity matched fluids where used ($M = 1$).

In [23], their best estimate of the exponent α when assuming the power law behavior $w_s \propto C_a^{-\alpha}$, was $\alpha = 0.6 \pm 0.2$. From our simulations on the lattice of 40×60 nodes we find $\alpha = 0.3 \pm 0.1$, which deviates from the result in [23], but is in agreement with simulations reported in [14]. For our simulations performed on the lattices of 25×35 nodes we also get $\alpha = 0.3 \pm 0.1$. A somewhat different process, but very interesting result, is given by Shaw in [25]. He measured the width of the drying front in a quasi two-dimensional porous system and found that $w_s \propto v_f^{0.48 \pm 0.1}$. Here v_f is the average front velocity. Quite recently, this has been compared to theory in [26].

The result of Wilkinson [10] in Eq. (2) gives in two dimension $\alpha = 0.38$, which lies within the uncertainties of our simulation results. However, we note that Fig. 15 shows a crossover in the scaling of the front width at $C_a \simeq 1.0 \times 10^{-5}$. When C_a is above this value, w_s of both experiments and simulations seems to scale with C_a

to the power 0.3. Below the crossover, $\alpha = 0.6$, is more consistent with the experimental results. We will propose to explain the crossover by the following arguments. In the previous sections we found that $\Delta P_{c\parallel} \propto \Delta h^\kappa$. The proportionality factor in this relation has not been discussed so far, but it is reasonable that it is proportional the injection rate Q . The injection rate sets the strength of the viscous pressure gradient resulting in the capillary pressure difference $\Delta P_{c\parallel}$. Thus, we obtain

$$\Delta P_{c\parallel} \propto C_a \Delta h^\kappa, \quad (8)$$

where our simulations show that $\kappa = 1.0 \pm 0.1$.

When gravity stabilizes the front the analog to Eq. (8) is $\Delta P_{c\parallel} \propto B_o \Delta h$. Thus, our simulation results indicate that $\Delta P_{c\parallel}$ varies linearly with Δh for both viscous and gravitational stabilization. Therefore, we suggest that when gravity is replaced by viscous forces we may simply substitute B_o with C_a .

In fact, Eq. (8) must lead to the conclusion that there is no difference between the evolution of the front in gravitational and viscous stabilization. In both cases the pressure gradient in the nonwetting fluid is constant across the width of the front. Therefore let us apply the same percolation concepts on the viscous process that was used in the gravitational case. At sufficiently low injection rate where the displacement is close to capillary equilibrium, the percolation theory gives $\Delta P_{c\parallel} \propto f - f_c \propto \xi^{-1/\nu}$ [13,10,11]. Here f is the occupation probability of the bonds, f_c is the percolation threshold of the lattice, and ξ is the correlation length ($\xi \propto w_s$). By inserting Eq. (8) for $\Delta P_{c\parallel}$ in the above relation, yields the power law $w_s \propto C_a^{-\nu/(1+\nu)}$. The exponent in this relation is exactly the same as the well known exponent in Eq. (1) for the gravity case. In two dimensions $\nu = 4/3$, giving $w_s \propto C_a^{-0.57}$, which is close to the experimental result of Frette *et al.* for low C_a in Fig. 15. We believe that the crossover at higher C_a is due to the dispersive growth of the front. At high injection rate the nonwetting fluid invades everywhere along the front and the displacement is far from capillary equilibrium. Consequently, the percolation method where always the bond with the highest occupation probability is the next to be invaded, is no longer a proper model for the displacement process. The fluctuations in the positions of the menisci inside the tubes may occasionally cause a more narrow tube to be invaded before a wider one. Therefore we expect another scaling of w_s at high $C_a \gtrsim 1.0 \times 10^{-4}$ as observed in Fig. 15. At lower $C_a \simeq 1.0 \times 10^{-5}$ the width of the front in our simulations becomes bounded by the lattice size and further reduction in C_a does not give rise to a wider front. Hence, with our simulations we are not able to observe the $w_s \propto C_a^{-0.57}$ regime. Note however, that the power law $\Delta P_{c\parallel} \propto \Delta h^\kappa$, where $\kappa = 1.0$ is found to be valid for both low and high capillary numbers.

V. CONCLUSION

We have reported on the stabilization process of the front width in drainage displacement going from low to high injection rates. The stabilization process was studied by using a network simulator that properly simulates the viscous and capillary pressure buildup in the fluids. We have found that the capillary pressure difference $\Delta P_{c\parallel}$, along the front varies linearly with the distance Δh , in the direction of the displacement. We conclude from simulations that $\Delta P_{c\parallel} \propto \Delta h^\kappa$ where our best estimate is $\kappa = 1.0 \pm 0.1$. This is not consistent with the theory proposed in [14], where they found $\kappa = 1 + t/\nu - \beta/\nu \approx 1.9$ in two dimensions.

In addition to $\Delta P_{c\parallel}$ we have calculated the capillary pressure fluctuations along the front in the direction parallel to the inlet, $\Delta P_{c\perp}$. Qualitatively, we have shown that $\Delta P_{c\perp}$ is a good indicator on whether the capillary pressures of the menisci along the front are all equal (capillary equilibrium) or fluctuating due to the viscous force field. When the capillary fluctuations are strong we do not expect invasion percolation to be a proper model for the displacement process.

We have also studied the scaling of the saturated front width w_s , as function of the capillary number C_a . As a consequence of the result $\Delta P_{c\parallel} \propto \Delta h^{1.0}$, we have shown that w_s must scale with C_a as $w_s \propto C_a^{-\nu/(1+\nu)}$. This is similar to what is known in gravitational stabilization where $w_s \propto B_o^{-\nu/(1+\nu)}$. We have also observed that experimental result of Frette *et al.* [23] is in better agreement with the scaling exponent $\nu/(1+\nu) \approx 0.57$ than the exponent in Eq. (2).

In Eqs. (2) and (3) t is a dynamic exponent depending on the conductivity of the lattice and with that also on the local current distribution [22]. The exponents β and ν , however, depend on the geometry of the structure only. Thus, the arguments in Refs. [10,14] that lead to Eqs. (2) and (3), combine dynamic and geometric exponents. We believe that such mixing of dynamic and geometric exponents, should be done with precaution for the following reasons. Experience with the random resistor network at the percolation threshold [27,28], shows that other dynamic exponents may be related in an extremely complex way. Attempts to derive them by simple arguments that combine dynamic and geometric exponents, fail. This is due to the multi-fractal structure of the current distribution. Presumably, this is also the case here, and for that reason the mixing of dynamic and geometric exponents fails to describe our simulation results.

ACKNOWLEDGMENTS

The authors thank E. G. Flekkøy for valuable comments. The work is supported by the Norwegian Research Council (NFR) though a “SUP” program and we acknowledge them for a grant of computer time.

APPENDIX A

Below we show how to deduce scaling relation (2) and find the exponent κ in the power law $\Delta P_{c\parallel} \propto \Delta h^\kappa$. The calculations are carried out in two dimension, however the extension to 3 dimensions is straight forward.

Let us consider a piece of the nonwetting phase of size Δh in the frontal region (see Fig. 1). We assume that $\Delta P_{c\parallel}$ vary as

$$\Delta P_{c\parallel} \propto v \Delta h^\kappa, \quad (\text{A1})$$

where v is the average fluid velocity in the pores. Moreover, we assume that the front has reached a steady state and that the structure of the front is similar to the front of the invasion cluster obtained in invasion percolation. This assumption provides that Δh is sufficiently large for the percolation concept to apply but less than the front width w_s .

The average nonwetting pore fluid velocity v , in the the region of size Δh , is given by Darcy's law

$$v = \frac{1}{S} \frac{k}{\mu} \frac{\Delta P_{c\parallel}}{\Delta h}. \quad (\text{A2})$$

Here S is the saturation of nonwetting phase, that is the volume fraction where nonwetting fluid can flow, and k is the permeability of the frontal region. According to percolation theory the frontal region is fractal with fractal dimension $D = d - \beta/\nu$, giving

$$S \propto \frac{\Delta h^{d-\beta/\nu}}{\Delta h^d} = \Delta h^{-\beta/\nu} \quad (\text{A3})$$

and

$$k \propto \Delta h^{-t/\nu}. \quad (\text{A4})$$

Here t is the conductivity exponent, β is the order parameter exponent and ν is the correlation length exponent in percolation theory.

By inserting the expressions for S , k and $\Delta P_{c\parallel}$ into Eq. (A2) we find the exponent $\kappa = 1 + t/\nu - \beta/\nu$. Scaling relation (2) follows by setting $\Delta h = w_s$ and replace $\Delta P_{c\parallel}$ in Eq. (A1) with the power law from percolation theory $w_s \propto \xi \propto \Delta P_{c\parallel}^{-\nu}$. Here ξ denote the correlation length in percolation theory.

- [4] M. Cieplak and M. O. Robbins, *Phys. Rev. Lett.* **60**, 2042 (1988).
- [5] P. G. de Gennes and E. Guyon, *J. Mec.* **17**, 403 (1978).
- [6] R. Chandler, J. Koplik, K. Lerman, and J. F. Willemsen, *J. Fluid Mech.* **119**, 249 (1982).
- [7] D. Wilkinson and J. F. Willemsen, *J. Phys. A* **16**, 3365 (1983).
- [8] R. Lenormand and C. Zarcone, *Phys. Rev. Lett.* **54**, 2226 (1985).
- [9] D. Wilkinson, *Phys. Rev. A* **30**, 520 (1984).
- [10] D. Wilkinson, *Phys. Rev. A* **34**, 1380 (1986).
- [11] A. Birovlev, L. Furuberg, J. Feder, T. Jøssang, K. J. Måløy, and A. Aharony, *Phys. Rev. Lett.* **67**, 584 (1991).
- [12] P. Meakin, A. Birovlev, V. Frette, J. Feder, T. Jøssang, K. J. Måløy, and A. Aharony, *Physica A* **191**, 227 (1992).
- [13] J.-F. Gouyet, B. Sapoval, and M. Rosso, *Phys. Rev. B* **37**, 1832 (1988).
- [14] B. Xu, Y. C. Yortsos, and D. Salin, *Phys. Rev. E* **57**, 739 (1998).
- [15] S. E. Buckley and M. C. Leverett, *Trans. Am. Inst. Min. Eng.* **146**, 107 (1942).
- [16] E. Aker, K. J. Måløy, A. Hansen, and G. G. Batrouni, *Transp. Porous Media* **32**, 163 (1998).
- [17] E. Aker, K. J. Måløy, A. Hansen, and G. G. Batrouni, *Phys. Rev. E* **58**, 2217 (1998).
- [18] W. B. Haines, *J. Agr. Sci.* **20**, 97 (1930).
- [19] K. J. Måløy, L. Furuberg, and J. Feder, *Phys. Rev. E* **53**, 966 (1996).
- [20] E. W. Washburn, *Phys. Rev.* **17**, 273 (1921).
- [21] G. G. Batrouni and A. Hansen, *J. Stat. Phys.* **52**, 747 (1988).
- [22] D. Stauffer and A. Aharony. *Introduction to percolation theory*. Taylor & Francis, London, Great Britain, 1992.
- [23] O. I. Frette, K. J. Måløy, J. Schmittbuhl, and A. Hansen, *Phys. Rev. E* **55**, 2969 (1997).
- [24] K. J. Måløy, L. Furuberg, J. Feder, and T. Jøssang, *Phys. Rev. Lett.* **68**, 2161 (1992).
- [25] T. M. Shaw, *Phys. Rev. Lett.* **59**, 1671 (1987).
- [26] I. N. Tsimpanogiannis, Y. C. Yortsos, S. Poulou, N. Kanellopoulos, and A. K. Stubos, *Phys. Rev. E* **59**, 4353 (1999).
- [27] L. de Arcangelis, S. Redner, and A. Coniglio, *Phys. Rev. B* **31**, 4725 (1985).
- [28] R. Rammal, C. Tannous, P. Breton, and A.-M. Tremblay, *Phys. Rev. Lett.* **54**, 1718 (1985).

- [1] K. J. Måløy, J. Feder, and T. Jøssang, *Phys. Rev. Lett.* **55**, 26881 (1985).
- [2] J.-D. Chen and D. Wilkinson, *Phys. Rev. Lett.* **55**, 1892 (1985).
- [3] R. Lenormand, E. Touboul, and C. Zarcone, *J. Fluid Mech.* **189**, 165 (1988).